## Energy materials

CrossMark

# Metal–organic-framework-derived Co/nitrogen-doped porous carbon composite as an effective oxygen reduction electrocatalyst

Tianrong Zhan[1,*] (ID), SiSi Lu[1] (ID), Haoqing Rong[1] (ID), Wanguo Hou[1] (ID),
Hongni Teng[2] (ID), and Yonghong Wen[1,*] (ID)

[1] Key Laboratory of Sensor Analysis of Tumor Marker (Ministry of Education), State Key Laboratory Base of Eco-chemical
Engineering, College of Chemistry and Molecular Engineering, Qingdao University of Science and Technology, Qingdao 266042,
China
[2] Department of Applied Chemistry, College of Chemical and Environmental Engineering, Shandong University of Science and
Technology, Qingdao 266510, China

## ABSTRACT

A Co-metal–organic-framework (MOF) crystal has been hydrothermally synthesized. Then the corresponding Co/nitrogen-doped porous carbon (Co/NPC) composite is fabricated by direct pyrolyzation of MOF without any precursor additive. The results reveal that the MOF-derived Co/NPC exhibits a porous structure with a surface area of 412 $m^2\ g^{-1}$ and a narrow pore size distribution (from 1.8 to 4.9 nm). The doped N mainly occurs in pyridine N and graphitic N types with total content as 4.11 at.%, which is originated from the N-based ligands in MOF. As an efficient oxygen reduction reaction (ORR) catalyst, Co/NPC shows a more positive onset potential (0.91 V vs. RHE) with a diffusion-limited current density of 5.46 mA $cm^{-2}$ at 0.3 V (vs. RHE). The rotating disk electrode and rotating ring-disk electrode results suggest that the Co/NPC catalyst experiences a nearly 4e pathway with a stronger methanol tolerance and better durability than commercial Pt/C catalyst in 0.1 M KOH. The excellent ORR catalytic activity of Co/NPC can be attributed to the N-doped porous carbon structure with incorporated metallic Co active species. This work affords a new strategy for preparation of non-noble metal ORR catalysts employing MOF as a precursor.

Address correspondence to E-mail: trzhan@sdu.edu.cn; yonghwen@163.com

## Introduction

The issues of global warming, environmental pollution and fossil fuels depletion have drawn much effort on clean and sustainable energy storage-conversion devices including fuel cells and metal–air batteries. Therein, electrochemical oxygen reduction reaction (ORR) is a crucial cathodic process for above renewable energy technologies [1–4]. Unfortunately, several disadvantages such as high overpotential and low efficiency as well as short lifetime greatly limit their large-scale commercialization due to the sluggish ORR kinetics. Although the advanced noble metal and their alloy nanohybrids (e.g., Pt, Pd and PtAu) have been developed as ORR catalysts with high activity and current density [5, 6], their prohibitive cost, scarcity and easy corrosion have hampered their widespread application in energy systems [7–9]. Thus, it is of significance to explore the efficient, earth-abundant and non-precious metal electrocatalysts for the large-scale commercialization of green energy devices.

The active transition metal (e.g., Co, Ni, Fe)-based porous carbon materials with heteroatom (e.g., N, S, P) doping/co-doping have shown excellent performance for ORR or oxygen evolution reactions (OER) and can be employed as one of the most likely alternative catalysts to noble metal nanomaterials [10–12]. Among the above mentioned electrocatalysts, cobalt-based nitrogen-doped porous carbon structures (e.g., graphene, carbon nanotubes) have demonstrated superior ORR activities for potential energy applications [13–16]. Thereof, porous carbon are much favorable for ORR activity due to its better stability, large surface area, fast kinetics, narrow pore size range, high pore volume and conductivity [13, 17]. Additionally, doping of N atom in carbon materials can enhance the current density and onset potential of ORR catalysis owing to the excellent electron-donor capacity and the plentiful nitrogen-involving active sites [12, 18]. It has been also well proven that the incorporation of Co transition metal into the N-doped carbon materials can further improve ORR performance of catalyst [19, 20]. Consequently, various Co-based N-doped carbon composites (e.g., Co/Co$_9$S$_8$@SNGS, Co@Co$_3$O$_4$/NC, Co$_3$O$_4$C-NA) [11, 18, 20–22] have been developed as effective ORR catalysts with higher stability and performance. Although inspired achievements, it is

still quite challenging to guarantee the uniformity of doped species (metal and nitrogen atoms) and the ordering of micro/mesoporous carbon materials, which are crucial to the mass transport and the accessibility of active sites.

Metal–organic frameworks (MOF) stand for a new class of porous crystalline materials, which are composed of metal ions or metal ion clusters and organic ligands [23, 24]. Given that the many unique merits including high surface area, porous structure and diverse composition, MOF have been extensively investigated for different applications ranging from gas separation and storage [25, 26], drug delivery [27], to catalysis [28, 29]. More importantly, the superiority of composition and structure allows MOF to be pyrolyzed as non-precious metal based porous carbons for ORR electrocatalysis [10, 30]. During pyrolysis process, the heteroatom (e.g., N) in organic ligands can be evenly doped into the MOF-derived carbon materials for improvement in catalytic performance [31]. Additionally, uniform metal ion in MOF scaffolds can lead to the well distributed active sites in N-doped porous carbon materials with larger specific surface area and higher electron transfer capability than MOF itself [32]. As a result, the synergistic effect between metal species and N-doped porous carbon can afford the high ORR performance because of superior conductivity, more catalytic active sites and porous structure. Above information has inspired us to develop high-efficiency metal/N-doped porous carbon from MOF networks as ORR electrocatalyst.

Herein, the Co/N-doped porous carbon (Co/NPC) composite was prepared by directly carbonizing our previously reported Co(O-BDC)(bbp) MOF crystals, which was hydrothermally synthesized by using 1,3-bis(benzoimidazol-2-yl)propane (bbp), 5-hydroxy-isophthalic acid (HO-H$_2$BDC), CoCl$_2$ and NaOH. The Co-MOF-derived Co/NPC products were carefully studied as ORR electrocatalyst. The results revealed that the Co/NPC catalyst exhibited the enhanced ORR catalytic activity relative to Co-MOF itself. The catalysis mechanisms were also analyzed on the basis of the experimental data.

# Experimental

## Chemicals

Nafion solution (5%) was obtained from DuPont Co. (USA). Polytetrafluoroethylene (PTFE, 60%, 0.20 μm) was supplied by Shenzhen Dechengwang S & T Ltd. Other reagents and chemicals were purchased from local shops as analytical pure. All of them were used as received without further purification.

## Preparation of catalyst Co/NPC

According to our previous procedure [33], the mixed aqueous solution were prepared by dissolving $CoCl_2 \cdot 2H_2O$, 1,3-bis(benzoimidazol-2-yl)propane (bbp), 5-hydroxyisophthalic acid (HO-$H_2$BDC) and NaOH in 20 mL DI water with their final concentrations as 0.05, 0.05, 0.05 and 0.15 M, respectively. Then the mixture was transferred into Teflon-lined stainless steel autoclaves for 72-h hydrothermal reaction at 160 °C. After cooling to room temperature, the MOF of $\{[Co(O\text{-}BDC)(bbp)] \cdot (H_2O)\}_n$ was afforded as pink crystals through filtration, washing and drying. The Co/NPC catalyst was prepared by direct carbonization of the MOF compound. Briefly, a ceramic boat containing the MOF compound was placed in a quartz tube of the furnace. Air was evacuated by 30-min continuous flow of highly pure $N_2$, and temperature was raised with rate of 5 °C/min to 250 °C for 2-h polymerization. Further carbonization was executed under $N_2$ atmosphere for 4 h at various temperatures (500, 600, 700 and 800 °C). The carbonized product was denoted as Co/NPC. Additionally, the Co/NPC at 600 °C was then leached in 3 M HCl at 80 °C for 4 h to remove unstable species from the catalysts. The responding product was named as NPC.

## Characterization of catalyst

X-ray diffraction patterns (XRD) were characterized on a Rigaku powder diffractometer equipped with Ni-filters Cu Kα radiation ($\lambda$ = 1.54050 Å, 40 kV and 100 mA). The morphology was executed by a JSM-6700F scanning electron microscope (SEM, Japan Electron Co.) and a JEOL JEM-2000EX transmission electron microscope (TEM, Japan Electron Co.). The BET specific surface areas are obtained by means of $N_2$ adsorption using an apparatus (Quantachrome-

Autosorb-1C, Quantachrome Instr., USA). The surface area and the pore size distribution were, respectively, calculated according to the liner part of the BET equation and the BJH method. XPS was conducted by using an HP 5950A ESCA spectrometer with an MgKa source.

## ORR electrocatalytic performance of Co/NPC

Electrochemical measurements were carried out on CHI 660D workstation in a conventional three-electrode cell. The Ag/AgCl (3 M) and platinum flake (1 × 2 cm$^2$) served as reference electrode and counter electrode, respectively. For preparation of working electrode, 10-mg as-synthesized catalyst was dispersed in 400 μL ethanol and 15 μL Nafion (1.0%) mixture by ultrasonic treatment for 15 min. Then 1 μL homogeneous ink was cast on a rotating disk electrode (RDE, $\emptyset$ = 2 mm), which was pretreatment by polishing and washing. Cyclic voltammetry (CV) was performed at a scan rate of 50 mV s$^{-1}$, and linear sweep voltammetry (LSV) was recorded at 10 mV s$^{-1}$ with various rotate speeds (400–2025 rpm). In all electrochemical experiments, 0.1 M KOH solution was acted as electrolyte and saturated with $O_2$ before each test. The reference potential relative to the reversible hydrogen electrode (RHE) was calculated basing on the Nernst equation [34]:

$$E_{RHE} = E_{Ag/AgCl} + 0.059 pH + 0.1976. \tag{1}$$

The exact kinetic parameters for the ORR activities, such as electron transfer number ($n$) and kinetic current density ($J_k$), were investigated according to the Koutecky–Levich (K–L) equation [35]:

$$\frac{1}{J} = \frac{1}{J_K} + \frac{1}{J_L} = \frac{1}{J_K} + \frac{1}{B \cdot \omega^{1/2}} \tag{2}$$

$$B = 0.62 \cdot n \cdot F \cdot C_0 \cdot D_0^{2/3} \cdot v^{1/6} \tag{3}$$

where $J$ is the measured current density, $J_k$ is the kinetic current density, $\omega$ is the electrode rotate speed, $n$ represents the number of electron transferred per oxygen molecule, $F$ is the Faraday constant (96485 C/mol), $D_0$ is the diffusion coefficient of $O_2$ in 0.1 M KOH (1.90 × 10$^{-5}$ cm$^2$ s$^{-1}$), $v$ is the kinematic viscosity of the electrolyte (0.01 cm$^2$ s$^{-1}$), and $C_0$ is the bulk concentration of $O_2$ (1.2 × 10$^{-6}$ mol/cm$^3$) [35]. The constant 0.2 is used when the rotate speed is expressed in rpm. For the rotating ring-disk electrode (RRDE) measurements, the %$HO_2^-$ and the electron

transfer number $n$ were determined by the following equations [36]:

$$\%HO_2^- = \frac{200 \cdot I_d}{N \cdot I_d + I_r} \tag{4}$$

$$n = 4I_d / \left( I_d + \frac{I_r}{N} \right) \tag{5}$$

where $I_d$ is the current of disk, $I_r$ is the current of ring, and $N$ is the current collection efficiency of the Pt ring. $N$ was determined to be 0.40 from the reduction in $K_3Fe(CN)_6$, well consisting with the manufacturer's value.

## Results and discussion

### Structural characterization of catalyst

The crystallinity of as-prepared Co-MOF and its Co/NPC are characterized by powder X-ray diffraction (XRD) patterns. As shown in Fig. 1a, the experimental XRD patterns of as-synthesized Co-MOF display the five strong diffractions peaks for (002), (100), (040), (21-1) and (15-1), which are highly matched with the calculated ones from its crystal data [33]. After directly pyrolyzing this template, Co/NPC (Fig. 1b) exhibits the distinct graphitic (002) and (101) plane diffraction peaks at 26.1° and 42.3° (JCPDS Card No. 75-1621), respectively [37]. Additionally, the diffraction reflections at 44.2° and 51.5° are attributed to the (111) and (200) crystalline planes of metallic Co (JCPDS card No. 96-900-8467) [38]. The diffraction peaks at 31.1° and 35.4° are assigned to (220) and (311) planes of $Co_3O_4$ [11] accompanying with a weak (111) reflection of CoO phase at 61.9°.
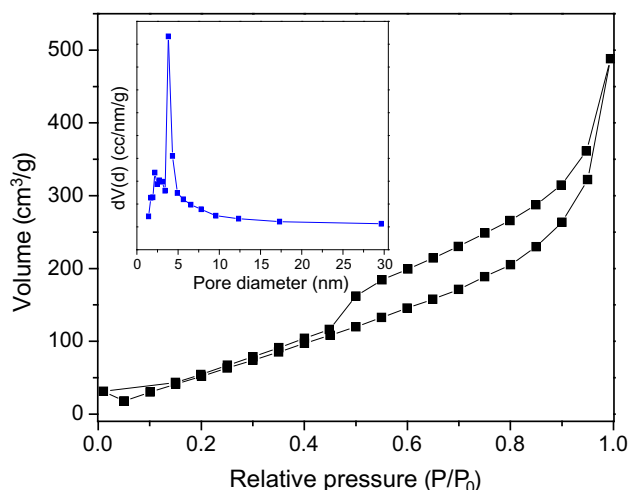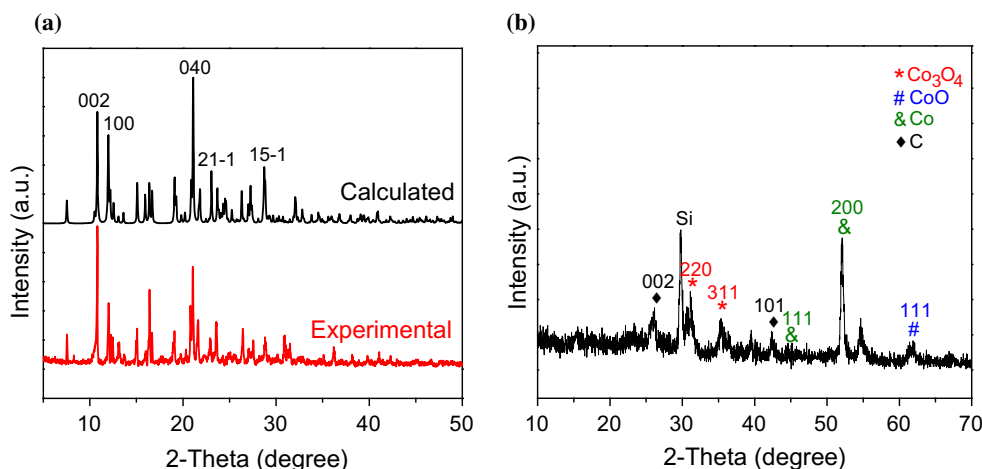


**Figure 2** Nitrogen adsorption–desorption isotherms of as-prepared Co/NPC and its pore size distribution (Inset).

The results reveal that Co-MOF has been converted into the graphitic carbon materials integrating various Co species including $Co_3O_4$, CoO and Co metal, which is favorable for ORR catalysis.

The texture properties of the resultant Co/NPC catalyst are investigated by using the nitrogen adsorption–desorption isotherms as shown in Fig. 2. The catalyst displays the classic IV adsorption/desorption isotherm with a well-defined H3-type hysteresis loop, which suggests existence of microporous and mesoporous structure. At a low relative pressure $P/P_0 < 0.1$, an obvious nitrogen uptake demonstrates the occurrence of micropores [39]. During $P/P_0$ range from 0.4 to 0.9, the hysteresis between adsorption and desorption branches indexes the characteristic of mesopores [40]. Correspondingly, Co/NPC shows a narrow pore size distribution between 1.8 and 4.9 nm
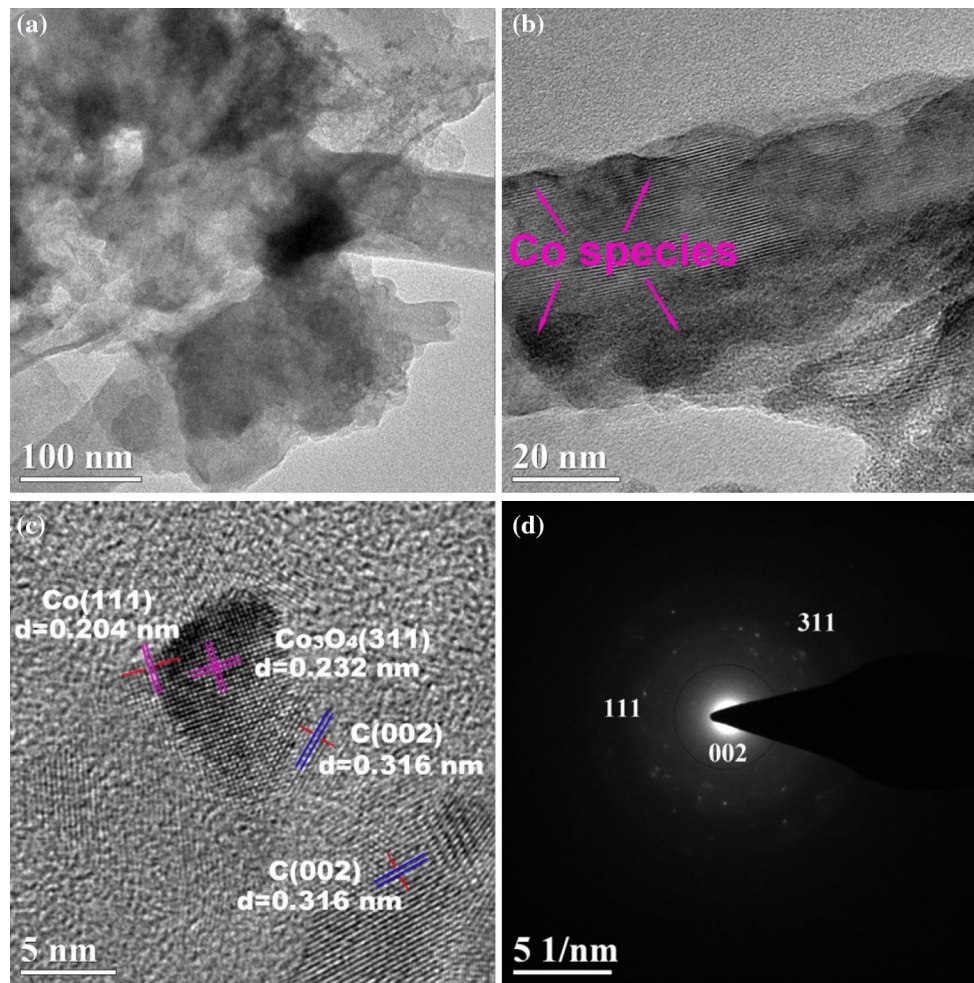
**Figure 1** The experimental and calculated powder XRD patterns of Co-MOF (**a**) and the XRD patterns of Co/NPC (**b**).

**Figure 3** TEM image (**a**), HRTEM images (**b** and **c**) and a selected area electron diffraction pattern **d** of Co/NPC catalyst.

with a total pore volume of 0.562 cm$^3$ g$^{-1}$ (Inset in Fig. 2), which is also confirmed by its TEM image in Fig. 3. The BET surface area of Co/NPC was obtained to be 412 m$^2$ g$^{-1}$, indicating the excellent porous structure derived from the well-ordered MOF precursor. It is supposed that the higher surface area and the abundance porosities can provide the more active sites for the faster electron communication and the lower mass transport resistance.

The porous morphology of Co/NPC is carefully characterized by TEM and HRTEM (Fig. 3). As shown in Fig. 3a, carbon materials predominantly appear in amorphous porous structure with some nanotube-shape moieties. The diameter of tube carbon species is around 40–70 nm, revealing formation of carbon nanotube. From the magnified TEM image in Fig. 3b, it can be found that there are distinct crystal lattice pattern of carbon on tube area. Moreover, some Co-based nanoparticles (dark subareas)

are incorporated in the carbon lamellar structures with uniform distribution. The HRTEM image in Fig. 3c shows Co species were encapsulated within the graphitic carbon layers. Therein, the most semi-transparent laminar morphology are ascribed to the ultrathin graphite carbon nanosheets with about 0.316 nm lattice fringe for (002) plane. Furthermore, the interplanar spacing values of 0.204 and 0.232 nm are responsible for the (111) lattice fringe of Co crystal and the (311) lattice fringe of Co$_3$O$_4$ phase [18]. The corresponding behaviors are presented in selected area electron diffraction (SAED) measurement (Fig. 3d), in which the Co/NPC composite are testified by the scattered dots (Co and Co$_3$O$_4$) and diffraction rings (graphitic carbon). The results are highly consistent with those of XRD. Given that these proof, we can confirm the successful preparation of Co/NPC nanocatalyst.

**Figure 4** Surface survey XPS spectrum (**a**), high-resolution C 1s XPS spectrum (**b**), high-resolution N 1s XPS spectrum (**c**) and high-resolution Co 2p XPS spectrum (**d**) of Co/NPC.
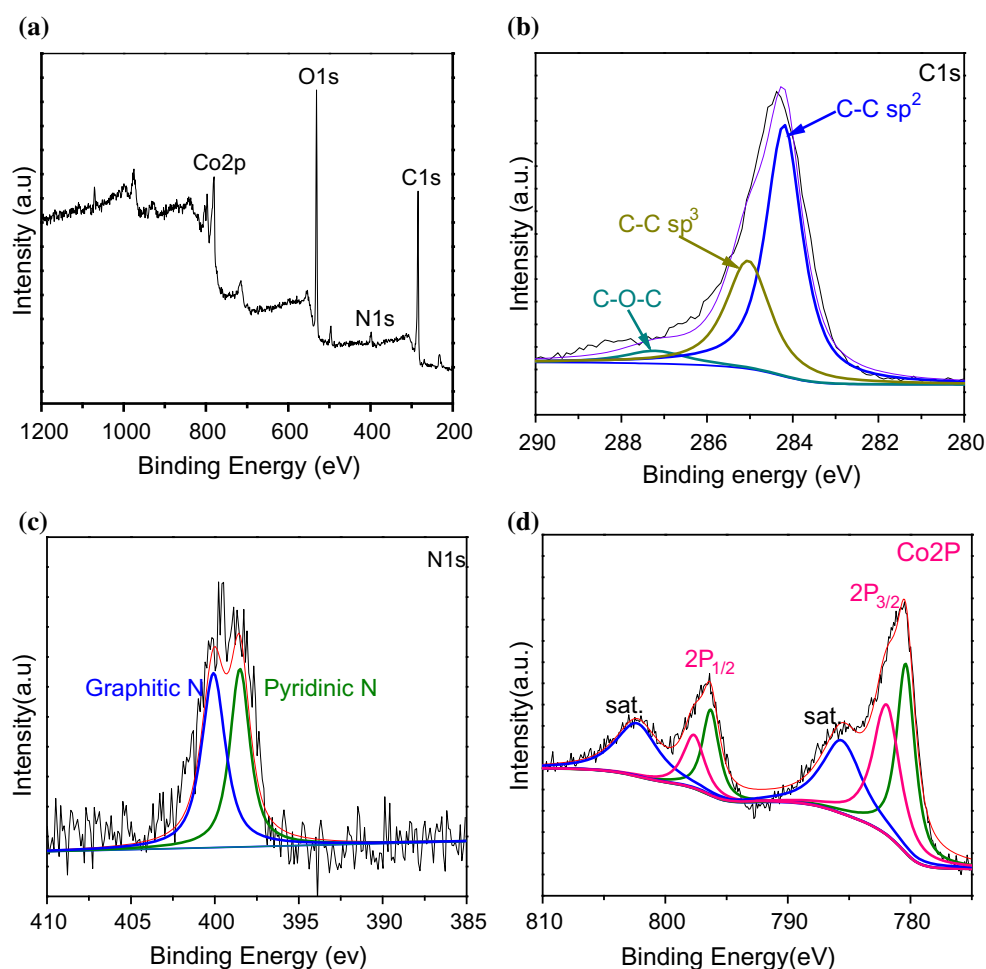
XPS measurements were then employed to characterize the chemical composition and elemental valence states of electrocatalyst. The survey spectrum in Fig. 4a demonstrates the existence of Co, O, N and C elements in Co/NPC composite with their sharp peaks at 780.1, 531.1, 398.1 and 284.1 eV, respectively. The contents of Co, O, N and C elements are, respectively, calculated to be 8.01, 33.26, 4.11 and 54.61 at.%, indicating successful transformation of Co-MOF to Co/NPC. In the high-resolution scan in Fig. 4b, C 1s spectra is deconvoluted into three different carbon species such as $sp^2$-hybridized graphite-like carbon (C=C) at 284.2 eV, $sp^3$-hybridized diamond-like carbon (C–C) at 285.1 eV, and a C–O–C bond at 287.4 eV [41, 42]. The predominant non-oxygenated C species (C=C and C–C) in catalyst are desirable to ORR activity owing to the enhanced graphitization. The N 1s spectrum in Fig. 4c is only deconvoluted to two peaks corresponding to the pyridinic N (398.5 eV) and graphitic N (400.1 eV)

components. It is well knowledge that both pyridine N and graphitic N are electroactive nitrogen types [43]. In fact, introduction of the doped N can afford more defects and surface polarity for excellent ORR performance because of its larger atomic radius than C [44]. The high electron donor nature derived from its lone pair electrons can result in convenient coordination of metal to form the favorable ORR active sites [45]. Figure 4d presents the best deconvolution of the Co 2p profile containing six peaks. Among them, the peaks at 785.7 and 802.5 eV are satellite peaks resulted from the shake-up excitation of the high-spin $Co^{2+}$ ions [46]. The XPS peak centered at 780.4 eV is assigned to Co $2p_{3/2}$ of $Co_3O_4$ in agreement with well-characterized $Co_3O_4$ crystal [11, 18]. The peak of Co $2p_{3/2}$ at 782.1 eV indexes the formation of $CoN_x$ and $CoO_x$ species in complexes form [17, 47]. The rest peaks at 796.4 and 797.7 eV are assigned to the characteristic of Co $2p_{1/2}$ species. The Co active species at various valence states

incorporated in catalyst can also be an enhancer for electrocatalytic activity [16].

## Electrochemical ORR

It is acknowledged that the ORR performances of catalysts are mainly reflected by their electrochemical behaviors. Firstly, the LSV curves of the four Co/NPC samples obtained at 500–800 °C were determined in $O_2$-saturated 0.1 M KOH medium as shown in Fig. S1. It is evident that the pyrolytic product at 600 °C gives rise to the biggest onset potential and diffusion-limited current. The effects of different loads for the Co/NPC product (at 600 °C) were also investigated as illustrated in Fig. S2. It can be easily seen that the loading of 0.49 mg $cm^{-2}$ is the optimal. Hence, the Co/NPC product (at 600 °C) with 0.49 mg $cm^{-2}$ loading was applied in the subsequent experiments. Then the CV curves of Co/NPC catalyst are determined in $O_2$- and $N_2$-saturated 0.1 M NaOH aqueous solution at scan rate of 10 mV $s^{-1}$ under the potential window from 0.2 to 1.1 V. As illustrated in Fig. 5a, the CV plot for $N_2$-saturated medium (black curve) does not appear any significant voltammetric current peak, revealing typical super capacitance performance [40]. However, in $O_2$-saturated electrolyte (red curve), a distinct well-defined cathodic peak at 0.79 V can be found, suggesting a high electrochemical activity of Co/NPC toward ORR in alkali solution [32]. The excellent ORR activity of Co/NPC could be also testified by LSV technique on RDE in 0.1 M KOH (Fig. 5b). It is obvious that the ORR onset potential and half-wave potential of Co/NPC (0.91

and 0.74 V) are both comparable to those of commercial 20% Pt/C catalyst (0.92 and 0.73 V). Furthermore, their diffusion-limited current densities at 0.30 V are almost equal (5.46 and 5.40 mA $cm^{-2}$ for Co/NPC and 20% Pt/C). However, the obtained Co/NPC hybrid highly outperforms the MOF precursor and metal free NPC counterparts. The results manifest that the significant ORR activity of Co/NPC is stemmed from the synergistic contribution of high conductive carbon layer and well-dispersed Co active species in doped carbon matrix as well as increased active sites owing to the N-atom self-doping [48].

For the sake of deep insight into ORR mechanism of the Co/NPC catalyst, LSV curves on RDE are also collected at rotation rate range from 400 to 2025 rpm (Fig. 6a). The limiting current density of catalyst is positively proportional to rotating speed, ascribing to the progressively reduced diffusion distance [12]. Obviously, the ORR of Co/NPC is subjected to a diffusion course at the potential more negative than 0.65 V and a mixed control process between 0.60 and 0.81 V [40]. Additionally, the Co/NPC catalyst follows the unchangeable overpotentials at different rotation speeds at the potential more positive than 0.81 V, divulging the superior initial ORR stability [49]. The corresponding K–L plots, depicting the relationship between reciprocal of current density against inverse of square root of rotating speed ($j^{-1}$ vs. $\omega^{-1/2}$), are obtained basing on the LSV curves data at different potentials as presented in Fig. 6b [12]. The K–L plots display the good linearity, suggesting the first-order ORR kinetics toward the dissolved oxygen concentration. It is also supported by
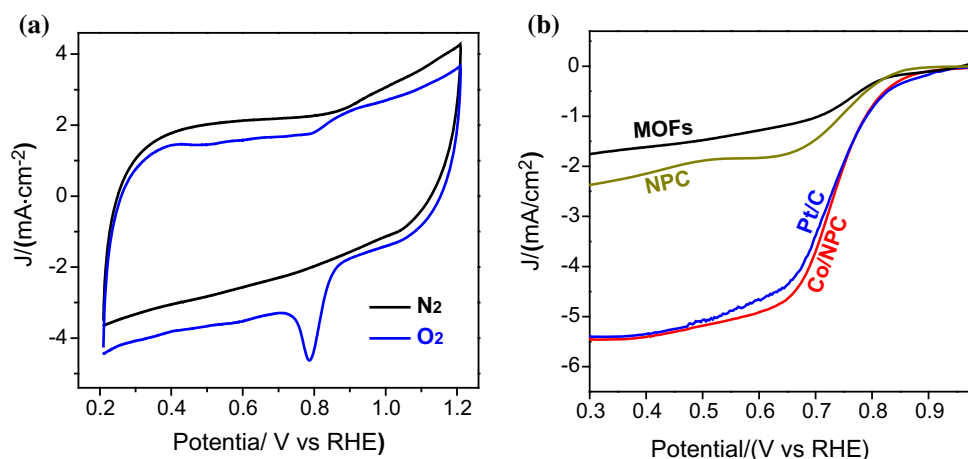


**Figure 5** **a** CVs in $N_2$- and $O_2$-saturated for Co/NPC catalyst and **b** LSV in $O_2$-saturated 0.1 M KOH for MOF, 20% NPC, Pt/C and Co/NPC catalysts at 1600 rpm.

**Figure 6  a** RDE voltammograms of Co/NPC in $O_2$-saturated 0.1 M KOH at a scan rate of 10 mV s$^{-1}$ at different rotating speed and **b** the corresponding K–L plot of $J^{-1}$ versus $\omega^{-1/2}$. The inset shows the electron transfer number ($n$). **c** RRDE voltammograms of Co/NPC in $O_2$-saturated 0.1 M KOH. The disk potential is scanned at 10 mV s$^{-1}$ and the ring potential is constant at 1.3 V. **d** The electron transfer number $n$ and percentage of $HO_2^-$ at certain potentials based on the corresponding RRDE results.
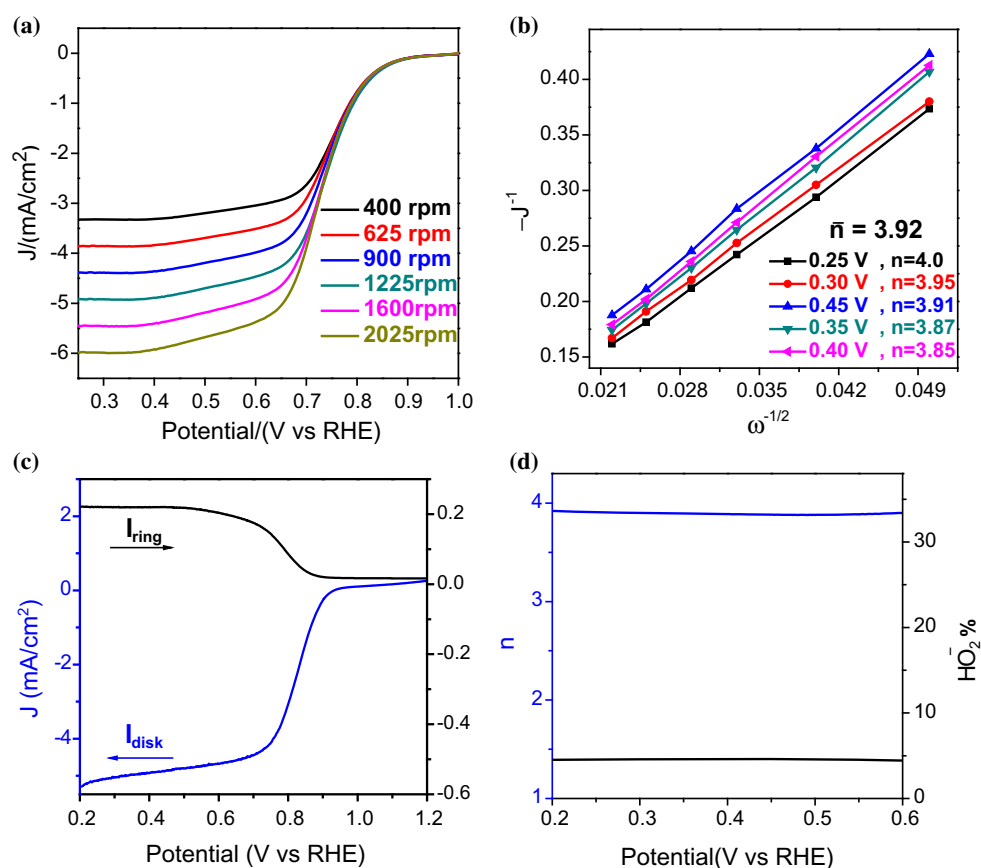


the similar electron transfer numbers from 3.85 to 4.00 at various potentials [50]. The mean electron transfer number of 3.92 demonstrates that the Co/NPC catalyst can perform ORR in alkaline solution through a perfect 4e pathway. In other word, the Co/NPC can directly reduce oxygen into $OH^-$ almost without harmful $O_2H^-$ intermediate. This superiority is also reconfirmed by monitoring $O_2H^-$ yield and evaluating the electron transfer number per oxygen molecule by using the RRDE measurement. Figure 6c shows the disk and ring current densities of the Co/NPC by RRDE voltammograms. On the basis of the disk and ring current, the measured $O_2H^-$ yield is less than 5%, and the electron transfer number is ranged from 3.88 to 3.92 over the potential region of 0.20–0.60 V in Fig. 6d. This is highly in line with the LSV results based on RDE experiments, affirmably inferring that the ORR follows an efficient 4e process at Co/NPC in alkaline media.

The durability and tolerance toward methanol crossover are also essential parameters for high-efficiency ORR catalyst. Therefore, the long-time

stabilities of both Co/NPC and commercial Pt/C were determined in $O_2$-saturated 0.1 M KOH solution by chronoamperometry. Figure 7a reveals that the current of Co/NPC only decreases by about 5% after continuous ORR testing for 9.5 h at 0.50 V (vs. RHE). By contrast, the current of commercial Pt/C catalyst appears about 28% reduction in the same period. The prominent stability of the Co/NPC catalyst is also verified by its LSV curves in Fig. S3. Obviously, the LSV curve after continuous potential 5000 cycles almost keeps the initial shape. The better stability of Co/NPC can be attributed to its highly graphitized carbon network and the rich active sites involving the doped nitrogen. Wherein the C–N bonding rather than physical adsorption can strengthen its corrosion resistance and guarantee the persistence of active sites in the catalyst structure during continuous measurements [37, 40]. Additionally, the protection role of the carbon species on Co can also alleviate the degradation of Co/NPC catalyst [51]. The poor durability of Pt/C can be ascribed to the degradation of Pt nanoparticles because of the

**Figure 7 a** Current–time responses of Co/NPC and 20% Pt/C at a rotating rate of 1600 rpm in $O_2$ saturated 0.1 M KOH; **b** Current–time chronoamperometric responses of Co/NPC and 20% Pt/C at 0.5 V (vs. RHE) in 0.1 M KOH. The arrows indicate the addition of $O_2$ and methanol.
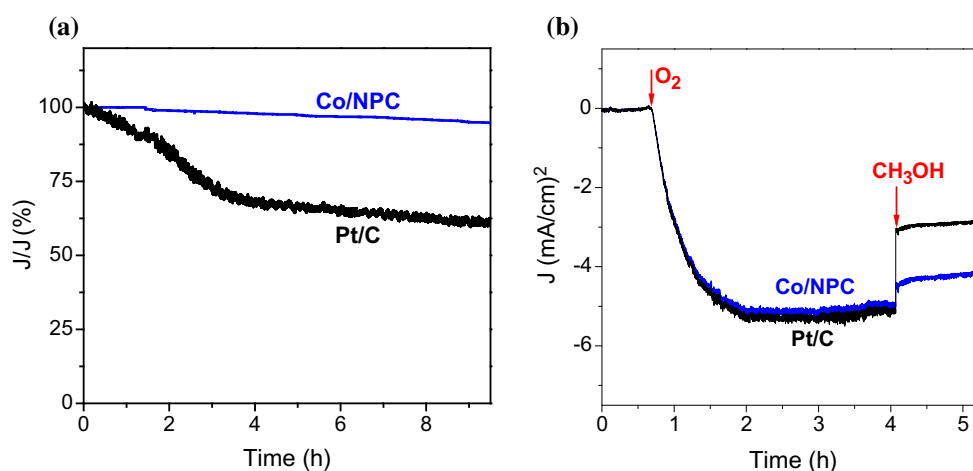


agglomeration and migration of Pt nanoparticles. Moreover, $i$–$t$ chronoamperometric curves of in $O_2$-saturated electrolyte in the presence of 2 M methanol were also recorded as presented in Fig. 7b. In the initial stage, addition of $O_2$ results in the distinct ORR current on both catalysts, meaning their good ORR activity. After injecting methanol, a dramatic drop is observed for Pt/C catalyst, while a slight decrease is detected under the similar experimental conditions. It is suggested that Co/NPC possesses superior tolerance ability against methanol poisoning. The above results manifest that Co/NPC has better methanol stability and tolerance than commercial 20 wt% Pt/C.

## Conclusion

A novel Co/NPC composite was successfully prepared through a direct pyrolysis of Co-MOF under $N_2$ atmosphere without adding any additive. The Co-MOF-derived Co/NPC displays microporous and mesoporous structures with large surface area and high percentage of pyridinic and graphitic nitrogen. Therefore, Co/NPC, as an efficient catalyst, presents excellent performance for ORR. The ORR electrochemical measurements demonstrate that Co/NPC displays the more positive onset potential and higher diffusion-limited current density in alkaline solution. Furthermore, the Co/NPC catalyst processes a perfect 4e mechanism with a small amount of $O_2H^-$ intermediates. The methanol tolerance and long-term durability of Co/NPC are also superior to those of Pt/C catalyst. It is suggested that the Co-MOF-derived Co/NPC can be a promising ORR catalyst for actual application.

## Compliance with ethical standards

**Conflict of interest** The authors declare that they have no conflict of interest.

**Electronic supplementary material:** The online version of this article (https://doi.org/10.1007/s10853-018-1989-x) contains supplementary material, which is available to authorized users.

## References

[1] Zhao S, Yin H, Du L, He L, Zhao K, Chang L et al (2014) Carbonized nanoscale metal–organic frameworks as high performance electrocatalyst for oxygen reduction reaction. ACS Nano 8:12660–12668

[2] Li Z, Sun H, Wei L, Jiang W, Wu M, Hu J (2017) Lamellar metal organic framework derived Fe–N–C non-noble electrocatalysts with bimodal porosity for efficient oxygen reduction. ACS Appl Mater Interfaces 6:5272–5278

[3] Walter MG, Warren EL, McKone JR, Boettcher SW, Mi QX, Santori EA et al (2010) Solar water splitting cells. Chem Rev 110:6446–6473

[4] Wang H, Dai H (2013) Strongly coupled inorganic-nano-carbon hybrid materials for energy storage. Chem Soc Rev 42:3088–3113

[5] Greeley J, Stephens IE, Bondarenko AS, Johansson TP, Hansen HA, Jaramillo TF et al (2009) Alloys of platinum and early transition metals as oxygen reduction electrocatalysts. Nat Chem 1:552–556

[6] Liang HW, Cao X, Zhou F, Cui CH, Zhang WJ, Yu SH (2011) A free-standing Pt-nanowire membrane as a highly stable electrocatalyst for the oxygen reduction reaction. Adv Mater 23:1467–1471

[7] Zhou L, Zhang C, Wei M, Evans DG, Duan X (2016) Directed growth of metal–organic frameworks and their derived carbon-based network for efficient electrocatalytic oxygen reduction. Adv Mater 28:2337–2344

[8] Wang E, Gu W, Hu L, Hong W, Jia X, Li J (2016) Noble-metal-free $Co_3S_4$-S/G porous hybrids as an efficient electrocatalyst for oxygen reduction reaction. Chem Sci 7:4167–4173

[9] Jian Z, Liu P, Li F, He P, Guo X, Chen M et al (2014) Core-shell-structured $CNT@RuO_2$ composite as a high-performance cathode catalyst for rechargeable $LiO_2$ batteries. Angew Chem Int Ed 53:442–446

[10] Ma M, You S, Gong X, Dai Y, Zou J, Fu H (2015) Silver/iron oxide/graphitic carbon composites as bacteriostatic catalysts for enhancing oxygen reduction in microbial fuel cells. J Power Sources 283:74–83

[11] Ma TY, Dai S, Jaroniec M, Qiao SZ (2014) Metal–organic framework derived hybrid $Co_3O_4$-carbon porous nanowire arrays as reversible oxygen evolution electrodes. J Am Chem Soc 136:13925–13931

[12] Zhan T, Liu X, Lu SS, Hou W (2017) Nitrogen doped NiFe layered double hydroxide/reduced graphene oxide mesoporous nanosphere as an effective bifunctional electrocatalyst for oxygen reduction and evolution reactions. Appl Catal B Environ 205:551–558

[13] Zhang C, Antonietti M, Fellinger TP (2014) Blood ties: $Co_3O_4$ decorated blood derived carbon as a superior bifunctional electrocatalyst. Adv Funct Mater 24:7655–7665

[14] Wu ZY, Chen P, Wu QS, Yang LF, Pan Z, Wang Q (2014) $Co/Co_3O_4$/C–N, a novel nanostructure and excellent catalytic system for the oxygen reduction reaction. Nano Energy 8:118–125

[15] Wang J, Wu H, Gao D, Miao S, Wang G, Bao X (2015) High-density iron nanoparticles encapsulated within nitrogen-doped carbon nanoshell as efficient oxygen electrocatalyst for zinc–air battery. Nano Energy 13:387–396

[16] Lu HS, Zhang H, Liu R, Zhang X, Zhao H, Wang G (2017) Macroscale cobalt-MOFs derived metallic Co nanoparticles embedded in N-doped porous carbon layers as efficient oxygen electrocatalysts. Appl Surf Sci 392:402–409

[17] Zhang X, Liu S, Zang Y, Liu R, Liu G, Wang G et al (2016) $Co/Co_9S_8$@S, N-doped porous graphene sheets derived from S, N dual organic ligands assembled Co-MOFs as superior electrocatalysts for full water splitting in alkaline media. Nano Energy 30:93–102

[18] Aijaz A, Masa J, Rösler C, Xia W, Weide P, Botz AJR et al (2016) $Co@Co_3O_4$ encapsulated in carbon nanotube-grafted nitrogen-doped carbon polyhedra as an advanced bifunctional oxygen electrode. Angew Chem Int Ed 55:4087–4091

[19] Han J, Sa YJ, Shim Y, Choi M, Park N, Joo SH et al (2015) Coordination chemistry of $[Co(acac)_2]$ with N-doped graphene: implications for oxygen reduction reaction reactivity of organometallic $CoO_4N$ species. Angew Chem Int Ed 54:12622–12626

[20] Sun T, Xu L, Li S, Chai W, Huang Y, Yan Y et al (2016) Cobalt–nitrogen-doped ordered macro-/mesoporous carbon for highly efficient oxygen reduction reaction. Appl Catal B Environ 193:1–8

[21] Niu KX, Yang BP, Cui JF, Jin JT, Fu XG, Zhao QP et al (2013) Graphene-based non-noble-metal Co/N/C catalyst for oxygen reduction reaction in alkaline solution. J Power Sources 243:65–71

[22] Lan YQ, Liu CH, Tang YJ, Wang XL, Huang W, Li SL et al (2016) Highly active Co–Mo–C/NRGO composite as efficient oxygen electrode for water–oxygen redox cycle. J Mater Chem A 4:418100–418106

[23] Furukawa H, Cordova KE, Keeffe MO, Yaghi OM (2013) The chemistry andapplications of metal–organic frameworks. Science 341:1230444–1230456

[24] Zhou HC, Long JR, Yaghi OM (2012) Introduction to metal–organic frameworks. Chem Rev 112:673–674

[25] Li JR (2009) Selective gas adsorption and separation in metal–organic frameworks. Chem Soc Rev 38:1477–1504

[26] Cadiau A, Adil K, Bhatt PM, Belmabkhout Y, Eddaoudi M (2016) A metal–organic framework-based splitter for separating propylene from propane. Science 353:137–140

[27] Horcajada P, Chalati T, Serre C, Gillet B, Sebrie C, Baati T et al (2014) Porous metal–organic-framework nanoscale carriers as a potential platform for drug delivery and imaging. Nat Mater 9:172–178

[28] Gao J, Miao J, Li J, Teng WY, Yang L, Zhao Y et al (2014) Ap-type Ti(IV)-based metal–organic framework with visible-light photo-response. Chem Commun 50:3786–3788

[29] Tanabe KK, Cohen SM (2011) Postsynthetic modification of metal–organic frameworks—a progress report. Chem Soc Rev 40:498–519

[30] Sun H, Su H, Ma X, Zhang P, Zhang X, Dai X et al (2016) Fe/IRMOF-3 derived porous carbons as non-precious metal electrocatalysts with high activity and stability towards oxygen reduction reaction. Electrochim Acta 205:53–61

[31] Xia BY, Yan Y, Li N, Wu HB, Lou XW, Wang X (2016) A metal–organic framework-derived bifunctional oxygen electrocatalyst. Nat Energy 1:15006–15009

[32] Yu H, Fisher A, Cheng D, Cao D (2016) Cu, N-codoped hierarchical porous carbons as electrocatalysts for oxygen reduction reaction. Acs Appl Mater Interfaces 8:21431–21439

[33] Wen YH, Xu GF, Yao K, Dou RT, Guo JX (2014) Syntheses, characterization, and electrochemical lithium-ion storage properties of two cobalt coordination polymers containing 5-hydroxyisophthalic acid and bis-benzoimidazole ligands. Z Anorg Allg Chem 640:2091–2096

[34] Ramírez A, Hillebrand P, Stellmach D, May MM, Bogdanoff P, Fiechter S (2014) Evaluation of MnO$x$, Mn$_2$O$_3$, and Mn$_3$O$_4$ electrodeposited films for the oxygen evolution reaction of water. J Phys Chem C 118:14073–14081

[35] Liu T, Guo YF, Yan YM, Wang F, Deng C, Rooney D et al (2016) CoO nanoparticles embedded in three-dimensional nitrogen/sulfur co-doped carbon nanofiber networks as a bifunctional catalyst for oxygen reduction/evolution reactions. Carbon 106:84–92

[36] Bian W, Yang Z, Strasser P, Yang R (2014) A CoFe$_2$O$_4$/-graphene nanohybrid as an efficient bi-functional electrocatalyst for oxygen reduction and oxygen evolution. J Power Sources 250:196–203

[37] Zhang LJ, Wang XY, Wang RH, Hong MC (2015) Structural evolution from metal–organic framework to hybrids of nitrogen-doped porous carbon and carbon nanotubes for enhanced oxygen reduction activity. Chem Mater 27:7610–7618

[38] Li R, Dai Y, Chen B, Zou J, Jiang BJ, Fu H (2016) Nitrogen-doped Co/Co$_9$S$_8$/partly-graphitized carbon as durable catalysts for oxygen reduction in microbial fuel cells. J Power Sources 307:1–10

[39] Hao GP, Lu AH, Dong W, Jin ZY, Zhang XQ, Zhang JT et al (2013) Sandwich-type microporous carbon nanosheets for enhanced supercapacitor performance. Adv Energy Mater 3:1421–1427

[40] Men B, Sun Y, Li M, Hu C, Zhang M, Wang L et al (2016) Hierarchical metal-free nitrogen-doped porous graphene/carbon composites as an efficient oxygen reduction reaction catalyst. Acs Appl Mater Interfaces 8:1415–1423

[41] Zhang L, Su Z, Jiang F, Yang L, Qian J, Zhou Y et al (2014) Highly graphitized nitrogen-doped porous carbon nanopolyhedra derived from ZIF-8 nanocrystals as efficient electrocatalysts for oxygen reduction reactions. Nanoscale 6:6590–6602

[42] Lu J, Zhou WJ, Wang LK, Jia J, Ke Y, Yang LJ et al (2016) Core–shell nanocomposites based on gold nanoparticle@Zinc–Iron-embedded porous carbons derived from metal–organic frameworks as efficient dual catalysts for oxygen reduction and hydrogen evolution reactions. ACS Catal 6:1045–1053

[43] Xia W, Mahmood J, Zou R, Xu Q (2015) Metal–organic frameworks and their derived nanostructures for electrochemical energy storage and conversion. Energy Environ Sci 8:1837–1866

[44] Wu G, Zelenay P (2013) Nanostructured nonprecious metal catalysts for oxygen reduction reaction. Acc Chem Res 46:1878–1889

[45] Gu WL, Hu LY, Li J, Wang EK (2016) Hybrid of g-C$_3$N$_4$ assisted metal–organic frameworks and their derived high-efficiency oxygen reduction electrocatalyst in the whole pH range. ACS Appl Mater Interfaces 8:35281–35288

[46] Tao L, Wang Q, Dou S, Ma Z, Huo J, Wang S et al (2016) Edge-rich and dopant-free graphene as a highly efficient metal-free electrocatalyst for the oxygen reduction reaction. Energy Environ Sci 52:2764–2767

[47] Olson TS, Pylypenko S, Atanassov P, Asazawa K, Yamada K, Tanaka H (2010) Anion-exchange membrane fuel cells: dual-site mechanism of oxygen reduction reaction in alkaline media on cobalt–polypyrrole electrocatalysts. J Phys Chem C 114:5049–5059

[48] Liu J, Sun X, Song P, Zhang Y, Xing W, Xu W (2013) High-performance oxygen reduction electrocatalysts based on cheap carbon black, nitrogen, and trace iron. Adv Mater 25:6879–6883

[49] Aravind SJ, Jafri RI, Rajalakshmi N, Ramaprabhu S (2011) Solar exfoliated graphene–carbon nanotube hybrid nano composites as efficient catalyst supports for proton exchange membrane fuel cells. J Mater Chem 21:18199–18204

[50] Liang Y, Li Y, Wang Y, Zhou J, Wang J, Regier T et al (2011) Co$_3$O$_4$ nanocrystals on graphene as a synergistic catalyst for oxygen reduction reaction. Nat Mater 10:780–786

[51] Hu H, Han L, Yu MZ, Wang ZY, Lou XW (2016) Metal–organic-framework-engaged formation of Co nanoparticle-embedded carbon@Co$_9$S$_8$ double-shelled nanocages for efficient oxygen reduction. Energy Environ Sci 9:107–111